Synthesis and Characterization of Highly Crystalline Graphene Aerogels

Marcus A. Worsley,[*,†] Thang T. Pham,[‡,§] Aiming Yan,[‡,§] Swanee J. Shin,[†] Jonathan R. I. Lee,[†] Michael Bagge-Hansen,[†] William Mickelson,[‡,∥] and Alex Zettl[‡,§,∥,⊥]

[†]Physical and Life Sciences Directorate, Lawrence Livermore National Laboratory, Livermore, California 94550, United States, [‡]Department of Physics, University of California, Berkeley, California 94720, United States, [§]Materials Science Division, Lawrence Berkeley National Laboratory, Berkeley, California 94720, United States, [∥]Center of Integrated Nanomechanical Systems, Berkeley, California 94720, United States, and [⊥]Kavli Energy NanoSciences Institute at the University of California, Berkeley, and the Lawrence Berkeley National Laboratory, Berkeley, California 94720 United States

ABSTRACT Aerogels are used in a broad range of scientific and industrial applications due to their large surface areas, ultrafine pore sizes, and extremely low densities. Recently, a large number of reports have described graphene aerogels based on the reduction of graphene oxide (GO). Though these GO-based aerogels represent a considerable advance relative to traditional carbon aerogels, they remain significantly inferior to individual graphene sheets due to their poor crystallinity. Here, we report a straightforward method to synthesize highly crystalline GO-based graphene aerogels *via* high-temperature processing common in commercial graphite production. The crystallization of the graphene aerogels *versus* annealing temperature is characterized using Raman and X-ray absorption spectroscopy, X-ray diffraction, and electron microscopy. Nitrogen porosimetry shows that the highly crystalline graphene macrostructure maintains a high surface area and ultrafine pore size. Because of their enhanced crystallinity, these graphene aerogels exhibit a ~200 °C improvement in oxidation temperature and an order of magnitude increase in electrical conductivity.

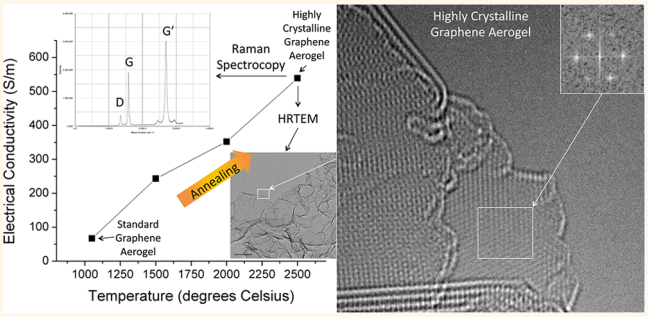

KEYWORDS: aerogel · graphene

Since its discovery, graphene has been a highly investigated material across a wide range of research fields.[1−8] Its exceptional properties, such as electrical conductivity of up to 10^4 S/cm, elastic modulus of up to 1 TPa, and surface area of over 2500 m^2/g have inspired applications in electronics,[1−3] conductive composites,[4] catalysis,[5] photovoltaics,[6] energy storage,[7] and biology.[8] Recent efforts to build three-dimensional (3D) architectures of graphene have demonstrated significantly enhanced performance due to increased active material per projected area.[9] Several methods have been proposed for building 3D graphene,[9] including chemical vapor deposition (CVD),[10,11] colloidal gelation,[12] sol−gel,[13−15] and graphene oxide (GO)-based gelation.[16−25] While CVD is the most common method for high quality two-dimensional (2D) graphene film growth,[2] the only 3D graphene structures available *via* CVD are macroporous foams due to limitations imposed by the requirement for growth on a metal support.[10] As a consequence, chemically derived GO-based graphene aerogels are the most common 3D graphene found in the literature due to their simple and versatile fabrication process and the ability to realize a wide range of pore morphologies, including ultrafine pore sizes (<100 nm).[16−26] The ultrafine pore sizes in aerogels are a key advantage over macroporous foams in a number of applications. For example, small pores have shown enhanced capacitance relative to larger pores, leading to performance enhancements in supercapacitor[27] and capacitive desalination[28,29] applications. Similarly, the small pore sizes and high surface areas inherent in aerogels have also proved advantageous in technologies, such as hydrogen storage,[30] catalysis,[31] batteries,[32] filtration,[33] insulation,[33,34] and sorbents.[35,36] In general, the GO-based graphene aerogels are formed by inducing the gelation of an aqueous GO suspension, such that the GO is partially reduced and forms a porous 3D network within the fluid.[26] Upon removal of

* Address correspondence to worsley1@llnl.gov.

Received for review September 19, 2014 and accepted October 5, 2014.

Published online October 06, 2014
10.1021/nn505335u

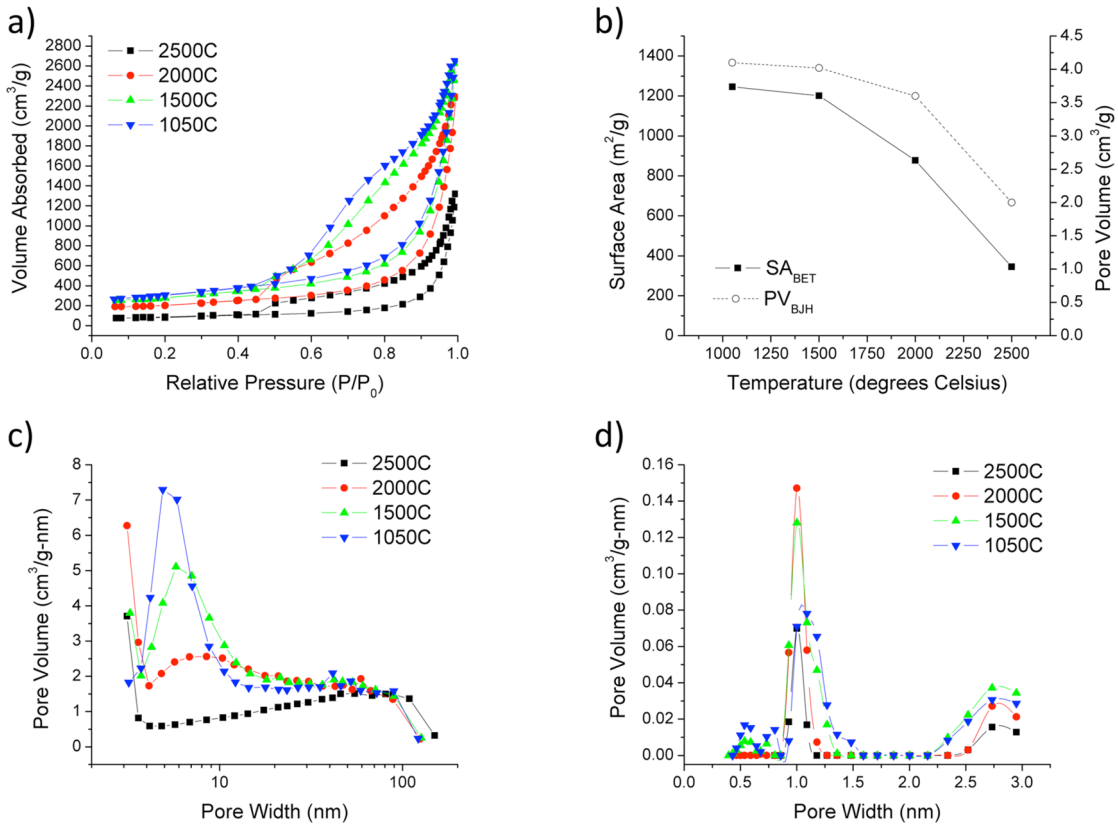

Figure 1. (a) Nitrogen adsorption−desorption isotherms for GMA at different annealing temperatures. b) GMA surface area (BET) and pore volume (BJH) *vs* annealing temperature. GMA pore size distributions in the (c) meso- and (d) micropore regimes.

the fluid phase *via* critical point drying (or freeze-drying), the dry 3D graphene emerges.[13,23−25] However, the quality of the graphene sheets in these chemically derived graphene aerogels is very poor compared to the graphene produced *via* mechanical exfoliation or CVD. The poor quality of the individual building units of the GO-based graphene aerogels translates to macroscale bulk properties, such as electrical conductivity, that are inferior to those of CVD-grown 3D graphene used in conductive polymer composites.[10] Therefore, methods are needed to improve the quality of the graphene sheets in chemically derived GO-based graphene aerogels.

Herein, we report a straightforward method for preparing chemical-derived GO-based graphene aerogels of a quality (*e.g.*, defect density, crystallinity, and domain size) approaching that of CVD-grown 3D graphene yet retaining the characteristic pore size distribution of chemically derived graphene aerogels. The general strategy involves subjecting a GO-based 3D graphene to high temperature annealing, similar to that used for the production of commercial graphite and carbon fibers,[37] as well as high quality graphene paper.[38] In this case, the graphene macroassembly (GMA)[22,23] is annealed at temperatures up to 2500 °C. In contrast to template-driven CVD-grown 3D graphene, which results in a macroporous foam, the annealed GMA possesses ultrafine pore sizes making it a true graphene aerogel. Moreover, the superior quality 2D graphene building blocks result in an order of magnitude improvement in bulk electrical conductivity *versus* previously reported graphene aerogels. Thus, the highly crystalline GMA exhibits conductivity on the order of CVD-grown macroporous graphene foam while maintaining significant pore volume in the submicron regime.

RESULTS AND DISCUSSION

The surface area and pore size of conventional aerogels have been shown to be sensitive to heat treatment.[31] Large losses in surface area are typically associated with coarsening of the primary particles in the aerogel network. Comparable losses have even been reported for traditional carbon aerogels.[39] Wiener *et al.* reported loss of surface area begins above 1000 °C for resorcinol−formaldehyde-derived carbon aerogels. Nitrogen porosimetry is a useful technique to observe the evolution of the pore morphology with temperature. Nitrogen adsorption/desorption isotherms for our GMA as a function of temperature (Figure 1a) are Type IV, indicative of mesoporous (pore diameters of 2−50 nm) material. The observation of a type 3 hysteresis loop (IUPAC classification) at high relative pressure is consistent with other 3D graphene materials.[14] The magnitude of the hysteresis between adsorption and desorption curves corresponds to the amount of pore volume present in the

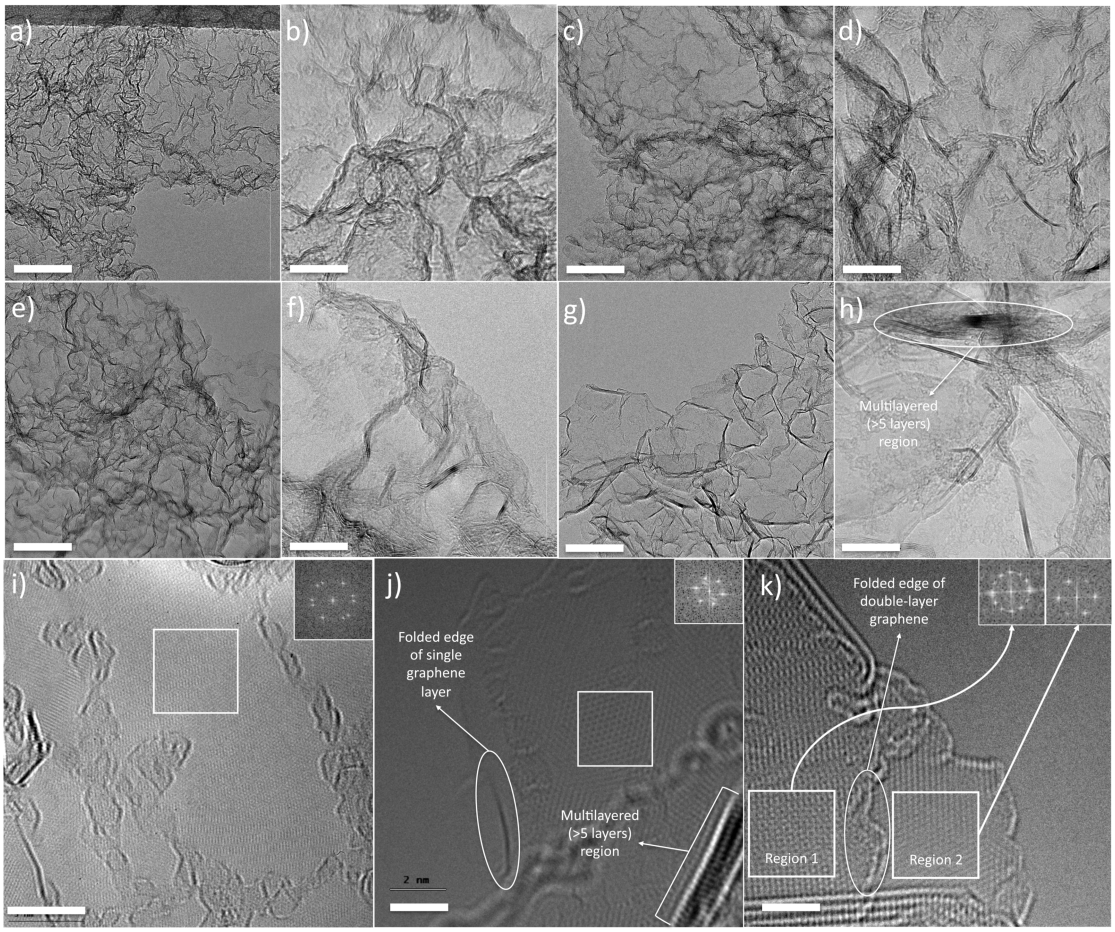

Figure 2. HRTEM images of GMA annealed at (a, b) 1050 °C, (c, d) 1500 °C, (e, f, i) 2000 °C, and (g, h, j, k) 2500 °C. Scale bar is 50 nm in (a), (c), (e), and (g). Scale bar is 10 nm in (b), (d), (f), (h), and (i). Scale bar is 2 nm in (j) and (k).

aerogel. The pore volume remains close to 4 cm^3/g at 1050 and 1500 °C. At 2000 °C it drops by 10% and then decreases to 2 cm^3/g at 2500 °C (Figure 1b). The trend in BET surface area behaves similarly. Surface area is approximately 1200 m^2/g at 1050 and 1500 °C, drops to 877 m^2/g at 2000 °C, and is further lowered to 345 m^2/g at 2500 °C. Pore size distributions in the meso- (2−50 nm) and micropore (<2 nm) regimes are also determined from the nitrogen isotherms as a function of temperature treatment (Figure 1 c,d). In the mesopore regime, the pore size distribution (PSD) exhibits a peak around 5 nm with a tail reaching to higher pore sizes at 1050 °C, which is characteristic of the GMA.[23] Above 1500 °C, a dramatic loss of the peak at 5 nm is observed as a function of temperature, though pores in the 20−100 nm range remain unchanged. In contrast, the micropore regime shows some changes in the intensity of the peak diameter around 1 nm with increasing heat treatment, but the general shape of the distribution is unchanged. Traditional carbon aerogels typically suffer large losses in both the meso- and micropore regimes above 1000 °C.[39] Therefore, these results suggest that the graphene aerogels are much more resistant to coarsening/sintering than traditional aerogels and able to maintain significant surface area and pore volume to much higher temperatures. The surface area and pore volume losses that are observed at 2000 and 2500 °C are a consequence of the loss of pores limited to the 2−10 nm regime. Remarkably, in contrast to traditional aerogels, pores in the 20−100 nm and sub-2 nm ranges remain intact and provide the considerable surface area measured in the annealed GMA up to 2500 °C.

High-resolution transmission electron microscopy (HRTEM) is also used to visualize the evolution of the pore morphology with temperature. Figure 2 presents low and high magnification images of the GMA after each heat treatment. At 1050 and 1500 °C, one observes the common "wrinkled sheet" network structure, with sheets primarily 1−3 layers thick (Figure 2a−d). The observed pore sizes are predominately sub-20 nm. At 2000 °C, one begins to observe changes in the wrinkled sheet morphology (Figure 2e,f,i) such as some flattening of the graphene sheets, and instead of curves, there are well-defined kinks with angles ranging from 110 to 170° that have emerged. Within the flatter layers the atoms appear to be highly ordered over length scales >10 nm as evidenced by the large-area Moiré pattern (Figure 2i). The Moiré pattern also indicates that though the layers in the few-layer

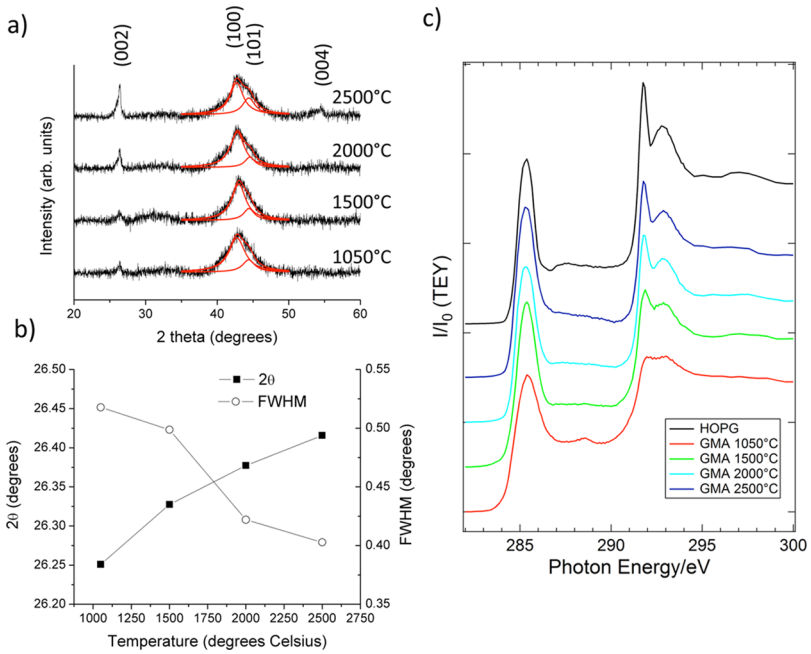

Figure 3. (a) XRD patterns for GMA at different annealing temperatures. Red lines denote peak fits for (100) and (101) diffraction peaks. (b) Plots of (002) diffraction angle and full width at half-maximum (fwhm) for GMA *vs* annealing temperature. (c) XAS spectra for GMA after annealing at different temperatures. Spectra offset for clarity.

graphene are well ordered, they are not perfectly aligned. Fast Fourier transform (FFT) analysis from selected areas of the HRTEM images indicates the angle of rotation between sheets is typically in excess of 10°. Figure 2i shows a typical HRTEM image of such a region, which has a rotation angle between graphene sheets of 15 ± 0.5°. In the GMA fired at 2500 °C, the material appears generally flatter than the material fired at 2000 °C and one observes sizable flat multilayered (>5 layers) regions as shown in Figure 2h. The atoms within each layer appear to be highly ordered, as observed for the GMA fired at 2000 °C (Figure 2j,k). Closer inspection reveals both single-layer graphene honeycomb lattice (also confirmed by the folded edge) with a length scale longer than 10 nm and multilayered (>5 layers) regions suggesting some graphitization of the GMA (Figure 2j). The inset in Figure 2j shows the FFT of the HRTEM image of the region outlined by the square, showing a single 6-fold symmetric diffraction pattern. Other regions are found to contain graphene sheets with a rotation angle between layers as shown in Figure 2k. The FFT of region 1 shows the rotation angle between the two layers of graphene is approximately 30° and the folded edge between regions 1 and 2 gives the information about the number of layers. Region 2 is single-layer graphene. Furthermore, the HRTEM images for 2500 °C show that the dominant pore size appears to shift above 20 nm. The increase in pore size with heat treatment is consistent with the PSD revealed from porosimetry measurements (Figure 1c) indicating a loss of the 2−10 nm pore with increasing temperature. At 2500 °C, porosimetry indicates that pores in the 20−100 nm range dominate, which is in excellent agreement with the HRTEM images. The observation of multilayers at high temperatures is consistent with the lower surface areas and pore volumes measured at 2500 °C. The flattening/kinking of the graphene sheets and long-range order (Moiré pattern) suggest significant crystallization at higher temperatures. Further characterization with more focused techniques will provide more details concerning crystallinity of the annealed GMAs.

X-ray diffraction (XRD) is an effective technique for probing the amount and orientation of graphitic carbon layers as well as the curvature of the individual sheets.[40] Figure 3 shows XRD patterns for the graphene aerogel after different heat treatments. All samples show a weak (002) peak at ∼26° compared to HOPG or bulk graphite[22,40] suggesting minimal stacking of sheets (predominantly single and few-layer graphene). The small increase in (002) peak intensity and the appearance of a weak (004) peak in samples annealed at 2500 °C indicates more stacking, which is consistent with the HRTEM images showing the appearance of regions with >5 layer stacks. Figure 3b also shows that the (002) full width at half-maximum (fwhm) decreases and (002) peak position increases with temperature. This is evidence of less graphene sheet curvature in the samples annealed at higher temperatures and is also supported by the appearance of the (004) peak[40] and the HRTEM results. It is also interesting to note the asymmetry in the (002) peak at 2000 and 2500 °C. This asymmetry is consistent with increased interlayer spacing due to the rotation between layers as observed in turbostratic graphite.[40] Lastly, there is an evolution in the broad (100)/(101) peak at 43−45° with increasing

temperature. Peak fits (Figure 3a) show an increase in the (101) peak intensity at 2500 °C. Li *et al.* report that an increase in the (101) peak intensity is evidence of more ordered stacking between layers (less rotation or translation).[40] Thus, all of the XRD results suggest a less defective graphene aerogel emerges after heat treatment while restacking of graphene layers is minimized.

X-ray absorption spectroscopy (XAS) is an angular momentum resolved probe of the unoccupied density of electronic states and, as such, can provide detailed information regarding local chemical bonding and insight into the quality and crystallinity of the graphene aerogel with heat treatment. Figure 3c displays XAS spectra recorded at the carbon K-edge for GMA heated to different annealing temperatures. All of the spectra exhibit features characteristic of highly sp^2-hybridized carbon. These features include a sharp resonance at ~285.4 eV arising to C(1s) → π^* transitions,[41] a resonance at ~291.5 eV that is attributed to a core-hole exciton state,[42] a broad onset to the core-hole exciton feature beginning at energies 289.5 eV and higher attributed to C(1s) → C−H σ^*/R* transitions,[41] and a series of broad resonances above 291.5 eV arising from C(1s) → C−C σ^* transitions. The as-prepared GMA exhibits an additional resonance at 288.5 eV that is attributed to C(1s) → C−O σ^* transitions, which is indicative of oxygen-based surface functionalities (*e.g.*, carboxyl, hydroxyl or epoxide groups).[43,44] Significantly, the intensity of this resonance is substantially diminished following annealing at 1500 °C and is completely absent from the XAS spectra after annealing at higher temperatures, providing a clear indication that the oxygen-based functional groups are successfully removed by thermal annealing.

The core−hole exciton feature and the broad onset that immediately precedes it are also observed to undergo pronounced changes as a function of the annealing temperature. More specifically, the intensity of the broad absorption onset substantially diminishes upon annealing of the GMA at temperatures of 1050 °C and above, indicating that the proportion of carbon bonded to hydrogen falls below the detection limits of the technique (~2%). Meanwhile, the core−hole exciton feature, which occurs due to the presence of extensive planar sheets of highly conjugated sp^2 carbon, is observed to sharpen and increase in intensity with increasing annealing temperature. This evolution in the core−hole exciton feature is consistent with an increase in the crystallinity and domain size of the graphene sheets within the GMA.[45,46] Equally, C−H bonds can only be present at domain edges or as defects in the graphene ligaments, and as such, the reduction in the C−H σ^*/R* resonances must arise due to an increase in domain size (reduction in the proportion of edge sites) or healing of defect sites under thermal annealing (increased crystallinity).

Raman spectroscopy is considered the gold standard for probing graphene due to its sensitivity to defects, chemical doping, and number of graphene layers present.[47,48] Raman spectra for typical GO-based graphene aerogels fired at <1500 °C (Figure 4a) look very similar to those of traditional carbon aerogels with strong, broad D and G bands and weak, ill-defined D′ and G′ bands.[14,39] Heat treatments of carbon aerogels at 2500 °C result in a sharpening of the bands, but the D band remains dominant,[39] indicative of nanocrystalline graphite.[49] In contrast, parts a and b of Figure 4 show that above 1500 °C, in addition to a significant sharpening of the peaks, there is an order of magnitude decrease in the D/G band intensity ratio. This dramatic decrease in D/G ratio indicates a removal of a considerable number of defects and is in agreement with decreased curvature seen in HRTEM and XRD results. The presence of a small D band at 2500 °C likely arises from the persistence of kinks and folds in the graphene sheets as seen in HRTEM. The D/G ratio is also an indicator of the crystallite size of the graphene sheets.[50,51] Larger crystallite size means larger single crystal graphene domains (*e.g.*, better crystallinity). Using the method pioneered by Tuinstra and Koenig,[50] Wiener *et al.* reported that traditional carbon aerogels show crystallite sizes increasing to ~5 nm at 2500 °C.[39] On the other hand, the graphene aerogels reported here show crystallite sizes >40 nm (Tuinsta and Koenig)[50] and as high as 150 nm using the method reported by Cancado *et al.*[51] (Figure 4c). Large graphene domains in the 20−100 nm range are consistent with observations in HRTEM and nitrogen porosimetry for the annealed GMA. This large crystallite size represents an order of magnitude improvement over traditional carbon aerogels or previously reported graphene aerogels.[14,39]

The Raman spectra of the graphene aerogels treated at 2000 and 2500 °C also reveal dramatic changes in the G′ band at ~2700 cm^{-1}. The G′/G band intensity ratio and the shape/position of the G′ band provide indicators of the number of layers and/or how well the layers are stacked. Single graphene layers have G′/G ratios >1, and the G′ band is a narrow, single peak.[47] Bulk graphite, few-layer, and bilayer graphene layers with ordered stacking have G′/G < 1, and the G′ band has a broad complex shape with a upshift in peak position compared to a single graphene sheet.[47] The upshift scales relative to the number layers in the stack. And finally, turbostratic graphite has G′/G ~1, and the *G′* band is a single, broadened peak with a large upshift relative to graphite.[47] Turbostratic graphite also has a D band. The graphene aerogel treated at 2000 and 2500 °C has a G′/G ≈ 1 (Figure 4a). The *G′* band is a single, broad (fwhm of 60 cm^{-1}) peak with a minimal shift (2698 ± 6 cm^{-1}) compared to single-layer graphene. This unique Raman signature appears to support the HRTEM results indicating few- and bilayer turbostratic (rotated) graphene. The decoupling of the layers due to rotation gives the G′/G ≈ 1 and peak broadening, while the minimal number of layers results in the minimal peak

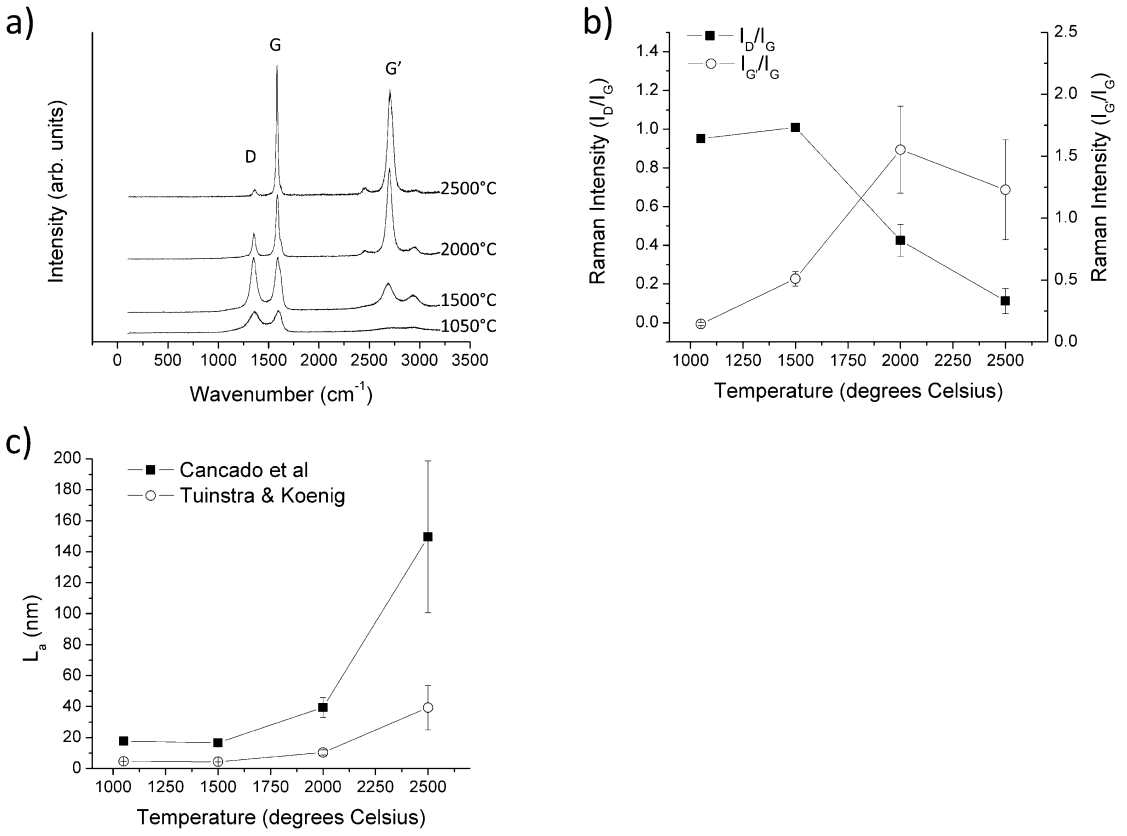

Figure 4. (a) Raman spectra for GMA after annealing at 1050, 1500, 2000, and 2500 °C. (b) Plot of Raman I_D/I_G and $I_{G'}/I_G$ for GMA *vs* annealing temperature and (c) crystallite size, L_a, of GMA as calculated according to methods by Cancado *et al.*[51] and Tuinstra and Koenig[50] *vs* annealing temperature.

shift relative to a single graphene. And finally, the high degree of crystallinity within each layer results in the diminished D band.

To date, the only report of such high quality Raman spectra from a three-dimensional graphene macrostructure required chemical vapor deposition (CVD) onto a macroporous metal foam substrate.[10] Because of the high level of graphene crystallinity in that structure, those authors reported good mechanical properties and order of magnitude improvements in electrical conductivity. Our GO-based graphene aerogel with ultrafine pore size also produced excellent mechanical properties, enhanced electrical conductivities, and robust thermal stability with the improvement in graphene quality. Thermal gravimetric analysis (TGA) in oxygen was performed on the GMA to determine its thermal stability in air. Figure 5a shows that as the GMA is annealed at higher temperatures, it becomes more resistant to oxidation in air. A quantitative determination of thermal stability was determined via the oxidation temperature, T_O (*i.e.*, the temperature of maximum rate of mass loss, Figure S1, Supporting Information). Figure 5b shows that T_O for the GMA increases from less than 600 °C for the standard GMA (1050 °C) to almost 800 °C after the 2500 °C anneal. This improvement of nearly 200 °C in thermal stability is due to the decreased defect density of the highly crystalline GMA and makes them suitable for high-temperature sensing and catalyst applications. Nanoindentation results (Figure 5c and Figure S2, Supporting Information) show that the modulus of the aerogel increases from ~90 to 143 MPa after the 2500 °C anneal. This increase in stiffness is a 50% improvement over the standard GMA (1050 °C) and 3−14 times larger than values previously reported for graphene aerogels with comparable densities (<100 mg/cm^3).[21,22] As the GMA does not exhibit significant densification with annealing, the ~50% improvement in stiffness is attributed to the larger, flatter crystalline domains present at 2500 °C. All samples exhibit primarily elastic behavior showing nearly full recovery after each loading−unloading cycle (Figure S2, Supporting Information). However, there were significant differences in the hysteresis loops, indicating changes in energy dissipation behavior with temperature. Figure 5c shows that the energy loss in the aerogel during compressive loading and unloading increases with temperature. The effective doubling in energy dissipation behavior by 2500 °C suggests enhanced performance for the highly crystalline GMA in energy absorbing applications. Four-point probe electrical measurements of the graphene aerogel show an increase in electrical conductivity of roughly an order of magnitude between GMA samples annealed at 1050

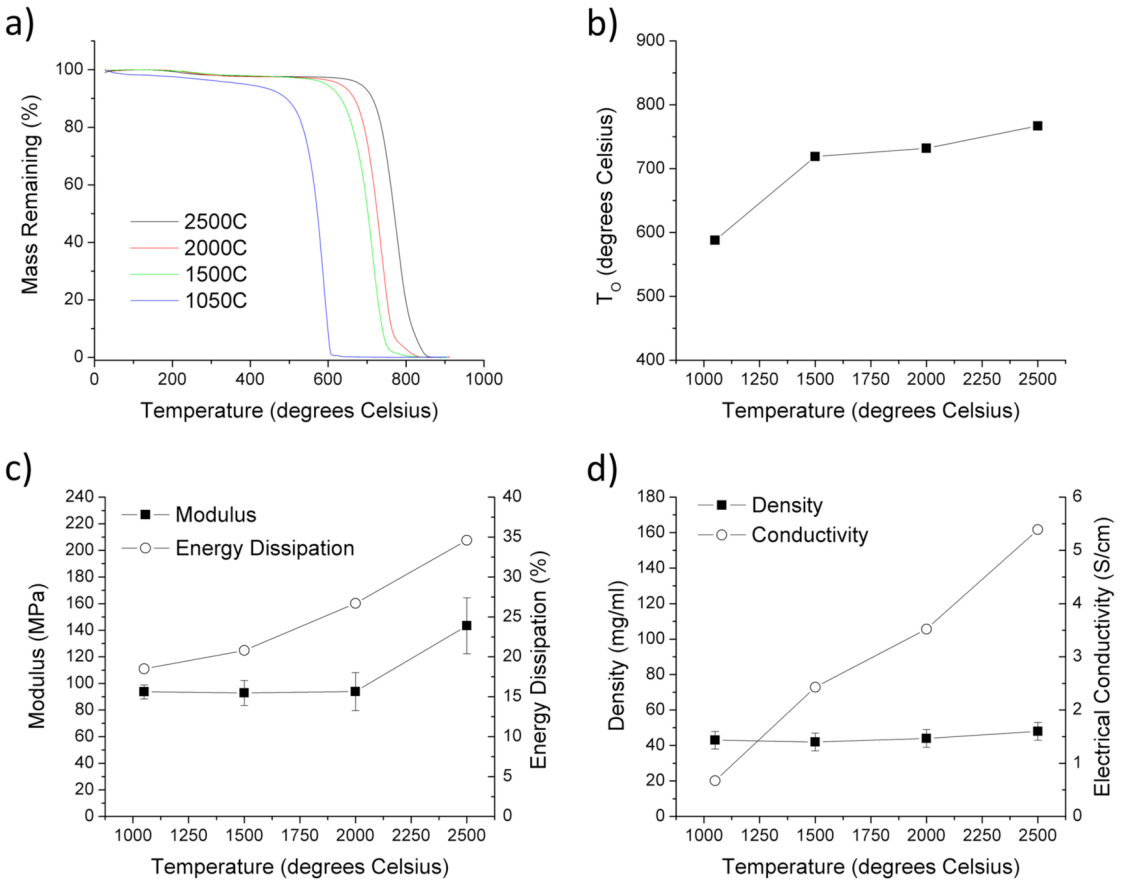

Figure 5. (a) TGA curves for the GMA treated at 1050, 1500, 2000, and 2500 °C. (b) Oxidation temperature, T_O, of GMA *vs* annealing temperature. (c) Young's modulus and energy loss for GMA *vs* annealing temperature. (d) Bulk density and electrical conductivity of GMA *vs* annealing temperature.

and 2500 °C, which increases linearly with annealing temperature and reaches >5 S/cm at 2500 °C (Figure 5d). This trend is in contrast to previous work showing no improvements in electrical conductivity above 1800 °C for carbon aerogels[39] and also represents a 2−10 fold increase over comparable graphene aerogels.[21,22] Moreover, the high electrical conductivity is on the order of that reported for the CVD-grown macroporous graphene foam.[10] In addition to polymer composite applications, this order of magnitude drop in resistance could be a game-changer for important energy technologies, such as capacitive deionization and fuel cells,[15] which could reap large energy efficiency gains from a lower resistance electrode.

CONCLUSION

In summary, we present a general strategy for producing high quality GO-based graphene aerogels via high-temperature annealing. These annealed GMAs maintained high surface area and ultrafine pore sizes even at temperatures up to 2500 °C. HRTEM shows that the annealed GMAs consist primarily of highly crystalline single and few-layer graphene. XRD studies confirm the removal of various defects with rising annealing temperature. Raman characterization is particularly informative, showing a steady decrease in defects and a marked increase in crystallite size with increasing temperature. Finally, it is observed that the improved quality of the graphene sheets in the annealed GMAs results in enhanced thermal stability and an order of magnitude increase in Young's modulus and bulk electrical conductivity compared to standard GO-based aerogels. With the already extensive and broad usage of GO-based aerogels in applications like supercapacitors, lithium ion batteries, biomimetics, and water remediation, the availability of CVD-grade GO-based graphene aerogels should facilitate significant performance enhancements for a wide range of technologies.

METHODS

Highly Crystalline Graphene Aerogel. Graphene aerogel samples were initially prepared according to a previous method.[22,23] All graphene macroassemblies (GMA) prepared according to this method received the standard thermal anneal at 1050 °C for 3 h in nitrogen. To prepare the highly crystalline GMA samples, the standard GMA was subjected to an additional thermal anneal for 1 h in He at 1500 °C, 2000 °C, or 2500 °C. Thus, GMA samples

treated at 1050, 1500, 2000, and 2500 °C were prepared and characterized according to the following methods.

Electron Microscopy. High-resolution transmission electron microscopy (HRTEM) characterization was performed on a JEOL JEM 2010 electron microscope and on TEAM 1.0, which is a double-aberration-corrected S/TEM with a resolution of 50 pm. All the HRTEM images were taken under TEM mode operated at 80 keV to minimize beam damage to the samples. The aerogels were sonicated in IPA and then dropcast onto lacey carbon TEM grids for analysis.

X-ray Absorption Spectroscopy. X-ray absorption spectroscopy (XAS) measurements were performed on beamline 8.0.1 of the Advanced Light Source, Lawrence Berkeley National Laboratory.[52] All XAS spectra were recorded at the carbon K-edge (from 280 to 330 eV) in the total electron yield mode via the drainage current from the experimental sample of interest. Calibration of the energy scale of BL8.0.1 was achieved by assigning an energy of 285.38 eV to the C(1s) $\rightarrow \pi^*$ resonance of a freshly cleaved sample of highly oriented pyrolytic graphite.[53] Each XAS spectrum was normalized to the incident flux (I_0), which was measured concurrently via the drainage current from a gold mesh located upstream of the experimental sample. In addition, the XAS spectra were normalized to the magnitude of the absorption edge step, which was taken as the difference in signal between the pre-edge (280 eV) and postedge (330 eV) regions. All XAS measurements were perfomed at an angle of incidence of 45° between the experimental sample and the incident X-ray beam.

Nitrogen Porosimetry. Textural properties were determined by Brunauer–Emmett–Teller (BET) and Barrett–Joyner–Halenda (BJH) methods using an ASAP 2020 surface area analyzer (Micromeritics Instrument Corp.) via nitrogen porosimetry.[54] Samples of approximately 0.1 g were heated to 300 °C under vacuum (10^{-5} Torr) for at least 24 h to remove all adsorbed species.

X-ray Diffraction. X-ray diffraction (XRD) measurements were performed on a Bruker AXS D8 ADVANCE X-ray diffractometer equipped with a LynxEye 1-dimensional linear Si strip detector. The samples were scanned from 5 to 75° 2θ. The step scan parameters were 0.02° steps and 2 s counting time per step with a 0.499° divergence slit and a 0.499° antiscatter slit. The X-ray source was Ni-filtered Cu radiation from a sealed tube operated at 40 kV and 40 mA. Phases in the samples were identified by comparison of observed peaks to those in the International Centre for Diffraction Data (ICDD PDF2009) powder diffraction database and also peaks listed in reference articles. Goniometer alignment was ensured using a Bruker-supplied Al_2O_3 standard.

Raman Spectroscopy. Raman spectra were collected using a Renishaw inVia spectrometer equipped with an Leica microscope (objective 50×) and a 514 nm Ar^+ laser (power of 9 mW) as the excitation source. In each scan, samples were exposed to the laser for 10 s (one accumulation), and the spectra were obtained in the range of 100–3200 cm^{-1} (Raman shift). The spectrometer was calibrated using a silicon standard, with a strong primary band at 520.5 cm^{-1}. Peak positions were fit assuming a Lorentz peak shape and a linear background.

Nanoindentation. The samples were indented in the load-controlled mode in an MTS XP nanoindenter with a Berkovich diamond tip. Elastic properties are characterized by the Young's modulus, which was calculated on the basis of the initial slope of the unloading curve according to the Oliver–Pharr method.[55] In Oliver–Pharr calculations, we assumed Poisson's ratios of diamond and the graphene assemblies of 0.07 and 0.2, respectively, and the Young's modulus of diamond of 1141 GPa.[56] Several (>10) indentations were performed on different sample locations and loading directions, and results were averaged. Standard deviation error was ±10%.

Thermal Gravimetric Analysis. Thermal gravimetric analysis (TGA) was performed on a PerkinElmer thermogravimetric analyzer. Each sample was heated in 20% O_2 (balance Ar) environment at a rate of 10 °C/min to at least 900 °C. The first derivative of each thermal decomposition curve was calculated to determine the temperature at which the maximum rate of decomposition occurred.

Electrical Conductivity. Electrical conductivity was measured using the four-probe method with metal electrodes attached to the samples. The amount of current transmitted through the sample during measurement was 100 mA, and the voltage drop along the various sample axes was measured over distances of 3 to 6 mm. Seven or more measurements were taken on each sample, and results were averaged.

Density. Bulk densities of the samples were determined from the physical dimensions and mass of each sample.

Conflict of Interest: The authors declare no competing financial interest.

Acknowledgment. This work was supported by the UC Lab Fees Research Program under Award No. 12-LR-235323; by Lawrence Livermore National Laboratory under the auspices of the U.S. Department of Energy under Contract No. DE-AC52-07NA27344, through LDRD Award No. 13-LW-099; by the National Science Foundation under the Center of Integrated Nanomechanical Systems Grant No. EEC-0832819; by the Director, Office of Basic Energy Sciences, Materials Sciences and Engineering Division, of the U.S. Department of Energy under Contract DE-AC02-05CH11231, within the sp^2-bonded Materials Program, and the National Center for Electron Microscopy of the Lawrence Berkeley National Laboratory, under Contract DE-AC02-05CH11231 (Proposal No. 1770), which provided for aberration corrected microscopy measurements. The Advanced Light Source is supported by the Director, Office of Science, OBES, of the US DoE under Contract No. DE-AC02-05CH11231.

Supporting Information Available: Plot of the mass loss rate (d*m*/d*T*) *vs* temperature for the GMA annealed at different temperatures and load *vs* displacement curves for GMA annealed at different temperatures. This material is available free of charge *via* the Internet at http://pubs.acs.org

REFERENCES AND NOTES

1. Novoselov, K. S.; Geim, A. K.; Morozov, S. V.; Jiang, D.; Zhang, Y.; Dubonos, S. V.; Grigorieva, I. V.; Firsov, A. A. Electric Field Effect in Atomically Thin Carbon Films. *Science* **2004**, *306*, 666–669.
2. Bae, S.; Kim, H.; Lee, Y.; Xu, X. F.; Park, J. S.; Zheng, Y.; Balakrishnan, J.; Lei, T.; Kim, H. R.; Song, Y. I.; *et al.* Roll-to-Roll Production of 30-Inch Graphene Films for Transparent Electrodes. *Nat. Nanotechnol.* **2010**, *5*, 574–578.
3. Schwierz, F. Graphene Transistors. *Nat. Nanotechnol.* **2010**, *5*, 487–496.
4. Stankovich, S.; Dikin, D. A.; Dommett, G. H. B.; Kohlhaas, K. M.; Zimney, E. J.; Stach, E. A.; Piner, R. D.; Nguyen, S. T.; Ruoff, R. S. Graphene-Based Composite Materials. *Nature* **2006**, *442*, 282–286.
5. Chen, D.; Tang, L. H.; Li, J. H. Graphene-Based Materials in Electrochemistry. *Chem. Soc. Rev.* **2010**, *39*, 3157–3180.
6. Guo, C. X.; Yang, H. B.; Sheng, Z. M.; Lu, Z. S.; Song, Q. L.; Li, C. M. Layered Graphene/Quantum Dots for Photovoltaic Devices. *Angew. Chem., Int. Ed.* **2010**, *49*, 3014–3017.
7. Yoo, J. J.; Balakrishnan, K.; Huang, J. S.; Meunier, V.; Sumpter, B. G.; Srivastava, A.; Conway, M.; Reddy, A. L. M.; Yu, J.; Vajtai, R.; *et al.* Ultrathin Planar Graphene Supercapacitors. *Nano Lett.* **2011**, *11*, 1423–1427.
8. He, S. J.; Song, B.; Li, D.; Zhu, C. F.; Qi, W. P.; Wen, Y. Q.; Wang, L. H.; Song, S. P.; Fang, H. P.; Fan, C. H. A Graphene Nanoprobe for Rapid, Sensitive, and Multicolor Fluorescent DNA Analysis. *Adv. Funct. Mater.* **2010**, *20*, 453–459.
9. Nardecchia, S.; Carriazo, D.; Ferrer, M. L.; Gutierrez, M. C.; del Monte, F. Three Dimensional Macroporous Architectures and Aerogels Built of Carbon Nanotubes and/or Graphene: Synthesis and Applications. *Chem. Soc. Rev.* **2013**, *42*, 794–830.
10. Chen, Z. P.; Ren, W. C.; Gao, L. B.; Liu, B. L.; Pei, S. F.; Cheng, H. M. Three-Dimensional Flexible and Conductive Interconnected Graphene Networks Grown by Chemical Vapour Deposition. *Nat. Mater.* **2011**, *10*, 424–428.
11. Mecklenburg, M.; Schuchardt, A.; Mishra, Y. K.; Kaps, S.; Adelung, R.; Lotnyk, A.; Kienle, L.; Schulte, K. Aerographite: Ultra Lightweight, Flexible Nanowall, Carbon Microtube Material with Outstanding Mechanical Performance. *Adv. Mater.* **2012**, *24*, 3486–3490.

12. Jung, S. M.; Jung, H. Y.; Dresselhaus, M. S.; Jung, Y. J.; Kong, J. A Facile Route for 3d Aerogels from Nanostructured 1d and 2d Materials. *Sci. Rep.* **2012**, *2*, 849.
13. Worsley, M. A.; Pauzauskie, P. J.; Olson, T. Y.; Biener, J.; Satcher, J. H.; Baumann, T. F. Synthesis of Graphene Aerogel with High Electrical Conductivity. *J. Am. Chem. Soc.* **2010**, *132*, 14067–14069.
14. Worsley, M. A.; Olson, T. Y.; Lee, J. R. I.; Willey, T. M.; Nielsen, M. H.; Roberts, S. K.; Pauzauskie, P. J.; Biener, J.; Satcher, J. H.; Baumann, T. F. High Surface Area, Sp2-Cross-Linked Three-Dimensional Graphene Monoliths. *J. Phys. Chem. Lett.* **2011**, *2*, 921–925.
15. Biener, J.; Stadermann, M.; Suss, M.; Worsley, M. A.; Biener, M. M.; Rose, K. A.; Baumann, T. F. Advanced Carbon Aerogels for Energy Applications. *Energy Environ. Sci.* **2011**, *4*, 656–667.
16. Bai, H.; Li, C.; Wang, X. L.; Shi, G. Q. A Ph-Sensitive Graphene Oxide Composite Hydrogel. *Chem. Commun.* **2010**, *46*, 2376–2378.
17. Chen, W.; Yan, L. In Situ Self-Assembly of Mild Chemical Reduction Graphene for Three-Dimensional Architectures. *Nanoscale* **2011**, *3*, 3132–3137.
18. Lin, Y.; Ehlert, G. J.; Bukowsky, C.; Sodano, H. A. Superhydrophobic Functionalized Graphene Aerogels. *ACS Appl. Mater. Interfaces* **2011**, *3*, 2200–2203.
19. Qiu, L.; Liu, J. Z.; Chang, S. L. Y.; Wu, Y. Z.; Li, D. Biomimetic Superelastic Graphene-Based Cellular Monoliths. *Nat. Commun.* **2012**, *3*, 1241.
20. Sun, H. Y.; Xu, Z.; Gao, C. Multifunctional, Ultra-Flyweight, Synergistically Assembled Carbon Aerogels. *Adv. Mater.* **2013**, *25*, 2554–2560.
21. Tang, Z. H.; Shen, S. L.; Zhuang, J.; Wang, X. Noble-Metal-Promoted Three-Dimensional Macroassembly of Single-Layered Graphene Oxide. *Angew. Chem., Int. Ed.* **2010**, *49*, 4603–4607.
22. Worsley, M. A.; Charnvanichborikarn, S.; Montalvo, E.; Shin, S. J.; Tylski, E. D.; Lewicki, J. P.; Nelson, A. J.; Satcher, J. H.; Biener, J.; Baumann, T. F.; *et al.* Toward Macroscale, Isotropic Carbons with Graphene-Sheet-Like Electrical and Mechanical Properties. *Adv. Funct. Mater.* **2014**, n/a–n/a.
23. Worsley, M. A.; Kucheyev, S. O.; Mason, H. E.; Merrill, M. D.; Mayer, B. P.; Lewicki, J.; Valdez, C. A.; Suss, M. E.; Stadermann, M.; Pauzauskie, P. J.; *et al.* Mechanically Robust 3d Graphene Macroassembly with High Surface Area. *Chem. Commun.* **2012**, *48*, 8428–8430.
24. Xu, Y.; Sheng, K.; Li, C.; Shi, G. Self-Assembled Graphene Hydrogel Via a One-Step Hydrothermal Process. *ACS Nano* **2010**, *4*, 4324.
25. Zhang, X.; Sui, Z.; Xu, B.; Yue, S.; Luo, Y.; Zhan, W.; Liu, B. Mechanically Strong and Highly Conductive Graphene Aerogel and Its Use as Electrodes for Electrochemical Power Sources. *J. Mater. Chem.* **2011**, *21*, 6494–6497.
26. Bai, H.; Li, C.; Wang, X.; Shi, G. On the Gelation of Graphene Oxide. *J. Phys. Chem. C* **2011**, *115*, 5545–5551.
27. Chmiola, J.; Yushin, G.; Gogotsi, Y.; Portet, C.; Simon, P.; Taberna, P. L. Anomalous Increase in Carbon Capacitance at Pore Sizes Less Than 1 Nanometer. *Science* **2006**, *313*, 1760–1763.
28. Porada, S.; Borchardt, L.; Oschatz, M.; Bryjak, M.; Atchison, J. S.; Keesman, K. J.; Kaskel, S.; Biesheuvel, P. M.; Presser, V. Direct Prediction of the Desalination Performance of Porous Carbon Electrodes for Capacitive Deionization. *Energy Environ. Sci.* **2013**, *6*, 3700–3712.
29. Kalluri, R. K.; Biener, M. M.; Suss, M. E.; Merrill, M. D.; Stadermann, M.; Santiago, J. G.; Baumann, T. F.; Biener, J.; Striolo, A. Unraveling the Potential and Pore-Size Dependent Capacitance of Slit-Shaped Graphitic Carbon Pores in Aqueous Electrolytes. *Phys. Chem. Chem. Phys.* **2013**, *15*, 2309–2320.
30. Liu, X. F.; Peaslee, D.; Jost, C. Z.; Baumann, T. F.; Majzoub, E. H. Systematic Pore-Size Effects of Nanoconfinement of Libh4: Elimination of Diborane Release and Tunable Behavior for Hydrogen Storage Applications. *Chem. Mater.* **2011**, *23*, 1331–1336.
31. Pajonk, G. M. Catalytic Aerogels. *Catal. Today* **1997**, *35*, 319–337.
32. Balaya, P. Size Effects and Nanostructured Materials for Energy Applications. *Energy Environ. Sci.* **2008**, *1*, 645–654.
33. Fricke, J.; Emmerling, A. Aerogels. *J. Am. Ceram. Soc.* **1992**, *75*, 2027–2036.
34. Lu, X.; Arduinischuster, M. C.; Kuhn, J.; Nilsson, O.; Fricke, J.; Pekala, R. W. Thermal-Conductivity of Monolithic Organic Aerogels. *Science* **1992**, *255*, 971–972.
35. Korhonen, J. T.; Kettunen, M.; Ras, R. H. A.; Ikkala, O. Hydrophobic Nanocellulose Aerogels as Floating, Sustainable, Reusable, and Recyclable Oil Absorbents. *ACS Appl. Mater. Interfaces* **2011**, *3*, 1813–1816.
36. Li, J. H.; Li, J. Y.; Meng, H.; Xie, S. Y.; Zhang, B. W.; Li, L. F.; Ma, H. J.; Zhang, J. Y.; Yu, M. Ultra-Light, Compressible and Fire-Resistant Graphene Aerogel as a Highly Efficient and Recyclable Absorbent for Organic Liquids. *J. Mater. Chem. A* **2014**, *2*, 2934–2941.
37. Acheson, E. G. Google Patents, **1896**.
38. Xin, G. Q.; Sun, H. T.; Hu, T.; Fard, H. R.; Sun, X.; Koratkar, N.; Borca-Tasciuc, T.; Lian, J. Large-Area Freestanding Graphene Paper for Superior Thermal Management. *Adv. Mater.* **2014**, *26*, 4521−+.
39. Wiener, M.; Reichenauer, G.; Hemberger, F.; Ebert, H. P. Thermal Conductivity of Carbon Aerogels as a Function of Pyrolysis Temperature. *Int. J. Thermophys.* **2006**, *27*, 1826–1843.
40. Li, Z. Q.; Lu, C. J.; Xia, Z. P.; Zhou, Y.; Luo, Z. X-Ray Diffraction Patterns of Graphite and Turbostratic Carbon. *Carbon* **2007**, *45*, 1686–1695.
41. Stohr, J. *Nexafs Spectroscopy*; Springer: New York, 1992.
42. Ma, Y.; Skytt, P.; Wassdahl, N.; Glans, P.; Guo, J.; Nordgren, J. Core Excitons and Vibronic Coupling in Diamond and Graphite. *Phys. Rev. Lett.* **1993**, *71*, 3725–3728.
43. Jeong, H. K.; Noh, H. J.; Kim, J. Y.; Jin, M. H.; Park, C. Y.; Lee, Y. H. X-Ray Absorption Spectroscopy of Graphite Oxide. *EPL* **2008**, *82*, 67004.
44. Jeong, H. K.; Noh, H. J.; Kim, J. Y.; Colakerol, L.; Glans, P. A.; Jin, M. H.; Smith, K. E.; Lee, Y. H. Comment on "Near-Edge X-Ray Absorption Fine-Structure Investigation of Graphene. *Phys. Rev. Lett.* **2009**, *102*, 099701.
45. Bernard, S.; Beyssac, O.; Benzerara, K.; Findling, N.; Tzvetkov, G.; Brown, G. E. Xanes, Raman and Xrd Study of Anthracene-Based Cokes and Saccharose-Based Chars Submitted to High-Temperature Pyrolysis. *Carbon* **2010**, *48*, 2506–2516.
46. Cody, G. D.; Alexander, C. M. O.; Yabuta, H.; Kilcoyne, A. L. D.; Araki, T.; Ade, H.; Dera, R.; Fogel, M.; Militzer, B.; Mysen, B. O. Organic Thermometry for Chondritic Parent Bodies. *Earth. Planet. Sci. Lett.* **2008**, *272*, 446–455.
47. Ferrari, A. C.; Meyer, J. C.; Scardaci, V.; Casiraghi, C.; Lazzeri, M.; Mauri, F.; Piscanec, S.; Jiang, D.; Novoselov, K. S.; Roth, S.; *et al.* Raman Spectrum of Graphene and Graphene Layers. *Phys. Rev. Lett.* **2006**, *97*, 187401.
48. Ferreira, E. H. M.; Moutinho, M. V. O.; Stavale, F.; Lucchese, M. M.; Capaz, R. B.; Achete, C. A.; Jorio, A.; , Evolution of the Raman Spectra from Single-, Few-, and Many-Layer Graphene with Increasing Disorder, *Phys. Rev. B 82* (**2010**).
49. Ferrari, A. C.; Robertson, J. Interpretation of Raman Spectra of Disordered and Amorphous Carbon. *Phys. Rev. B* **2000**, *61*, 14095–14107.
50. Tuinstra, F.; Koenig, J. L. Raman Spectrum of Graphite. *J. Chem. Phys.* **1970**, *53*, 1126–&.
51. Cancado, L. G.; Takai, K.; Enoki, T.; Endo, M.; Kim, Y. A.; Mizusaki, H.; Jorio, A.; Coelho, L. N.; R. Magalhaes-Paniago Pimenta, M. A.; , General Equation for the Determination of the Crystallite Size L-a of Nanographite by Raman Spectroscopy, *Appl. Phys. Lett. 88* (**2006**).
52. Jia, J. J.; Callcott, T. A.; Yurkas, J.; Ellis, A. W.; Himpsel, F. J.; Samant, M. G.; Stohr, J.; Ederer, D. L.; Carlisle, J. A.; Hudson, E. A.; *et al.* First Experimental Results from Ibm/Tenn/Tulane/Llnl/Lbl Undulator Beamline at the Advanced Light-Source. *Rev. Sci. Instrum.* **1995**, *66*, 1394–1397.
53. Batson, P. E. Carbon 1 < I>S</I> near-Edge-Absorption Fine Structure in Graphite. *Phys. Rev. B* **1993**, *48*, 2608–2610.

54. Gregg, S. J.; Sing, K. S. W. *Adsorption, Surface Area, and Porosity*, 2nd ed.; Academic Press: London, 1982.
55. Oliver, W. C.; Pharr, G. M. An Improved Technique for Determining Hardness and Elastic-Modulus Using Load and Displacement Sensing Indentation Experiments. *J. Mater. Res.* **1992**, *7*, 1564–1583.
56. Kucheyev, S. O.; Hamza, A. V.; Satcher, J. H.; Worsley, M. A. Depth-Sensing Indentation of Low-Density Brittle Nanoporous Solids. *Acta Mater.* **2009**, *57*, 3472–3480.